



## Effect of gasket material on flange face corrosion

Soroosh Hakimian, Abdel-Hakim Bouzid, Lucas A. Hof\*

Mechanical Engineering Department, École de Technologie Supérieure, 1100, Rue Notre-Dame Ouest, Montreal, Québec, H3C 1K3, Canada

### ARTICLE INFO

#### Keywords:

Flange corrosion  
Gasket material  
Crevice corrosion  
Galvanic corrosion

### ABSTRACT

Bolted flanged joints play a crucial role in connecting pressure vessels and piping systems. The corrosion of the flange surface is one of the most common causes of leakage failure in bolted flanged joints. This research investigates the effect of three gasket materials on the corrosion behavior of 321 stainless steel flange material using a novel setup specially designed for corrosion quantification of such assemblies. The results show that graphite gaskets cause more corrosion to flange surfaces under the same working conditions compared to graphite gaskets with metal foil inserts and virgin polytetrafluoroethylene (PTFE) gaskets. The mechanism of flange face corrosion is that, for PTFE gaskets, corrosion propagation mainly occurs at the gasket inner diameter and propagates through the depth of the flange while, for graphite gaskets, corrosion occurs on the whole contact surface of the flange and the gasket.

### 1. Introduction

A bolted flanged joint (BFJ) is a type of a seal device that connects pressure vessels and piping components by means of flanges, gaskets, and bolts [1]. These types of joints are frequently used in industrial installations where there is a need to connect pipelines or pressure vessels that handle fluids under high pressure and temperature conditions, such as boilers, condensers, heat exchangers, reactors, steam generators, and piping systems [2]. Ease of assembly and disassembly for maintenance and repair services is the advantage of this type of connection compared to welded joints [3]. However, it also has the potential to fail due to leaks, particularly when exposed to harsh and corrosive environments at high temperatures and pressures [4].

The frequent premature leakage failure of BFJ due to corrosion in different industrial applications necessitates the analysis of failure root causes and mechanisms [5]. The flange face corrosion usually occurs at the interface of the flange and gasket, where the corrosive solution can penetrate the gap between the two flange faces or between the flange and gasket [6]. These gaps are created by material loss due to corrosion and aging and facilitated by the loosening of the joint due to the creep-relaxation of the joint [7,8], rotation on the flange [9,10], and waviness and misalignment [11,12]. Documented instances of premature corrosion failures mentioned that galvanic [13] and crevice corrosion [14] are the most repeated types of corrosion in these joints. Galvanic corrosion accelerates the flange face corrosion in cases where metallic gaskets [15], semi metallic gaskets [16], or graphite sheet

gaskets [17] are used in conjunction with flanges. Flange face corrosion compromises the necessary smoothness and evenness required for effective sealing. As a result, the joint may fail to maintain uniform pressure distribution on the gasket, resulting in leakage of pressurized fluid [18].

Metallurgical factors [18], environmental conditions [14], gap or crevice geometry [19], and the flange and gasket materials [20,21] have an influence on the flange corrosion behavior. Tavares et al. [18] reported that an inadequate chemical composition and microstructure of the flange material were the main reasons for an UNS S32750 flange corrosion failure. In another study, Kolblinger et al. [14] demonstrated that the presence of bacteria in seawater caused microbiological-induced crevice corrosion (MIC) on an UNS S32760 superduplex steel flange face, although the microstructure and fabrication process were according to the ASTM A182 standard. The size of the gap, or crevice, is a significant factor in the initiation and development of crevice corrosion [22]. A recent study analyzed the effect of PTFE gasket size on the flange face corrosion in a 3.5 wt% NaCl solution at 50 °C, and the results showed that decreasing the gasket thickness have a significant effect on the initiation of crevice corrosion [19].

Material selection is a crucial step in the design of engineering structures, as it determines the adequacy of the structure corrosion lifetime considering the environment to which it is exposed [23]. Therefore, the importance of studying the effect of flange and gasket materials on the flange face corrosion is acknowledged. Martin et al. [24] compared the crevice corrosion initiation and propagation of

\* Corresponding author.

E-mail addresses: [soroosh.hakimian.1@ens.etsmtl.ca](mailto:soroosh.hakimian.1@ens.etsmtl.ca) (S. Hakimian), [hakim.bouzid@etsmtl.ca](mailto:hakim.bouzid@etsmtl.ca) (A.-H. Bouzid), [lucas.hof@etsmtl.ca](mailto:lucas.hof@etsmtl.ca) (L.A. Hof).

<https://doi.org/10.1016/j.ijpvp.2024.105207>

Received 17 October 2023; Received in revised form 25 April 2024; Accepted 7 May 2024

Available online 9 May 2024

0308-0161/© 2024 The Authors. Published by Elsevier Ltd. This is an open access article under the CC BY license (<http://creativecommons.org/licenses/by/4.0/>).

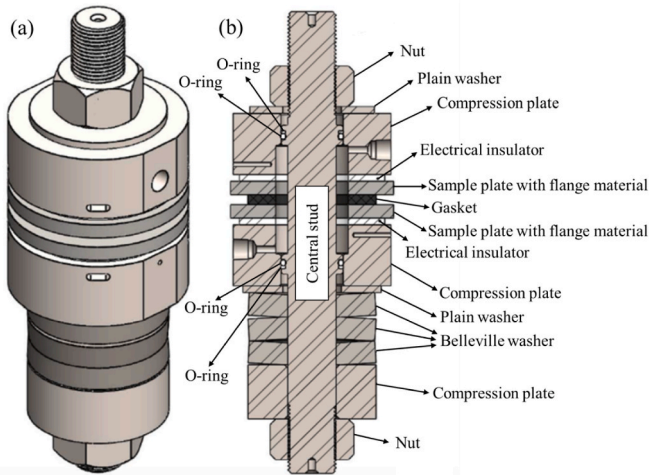


Fig. 1. Test fixture (a) 3D view (b) cross section view and labelling of each item (adapted from Ref. [28]).

different Ni–Cr–Mo alloys in seawater at 65 °C. This study deployed the pitting resistance equivalent number (PREN) method to find a correlation with the crevice corrosion penetration rate. It was reported that the higher the PREN, the lower the crevice penetration rate, at a constant polarized potential of 300 mV (Ag/AgCl) and 65 °C of seawater. The effect of temperature, chlorination, and the flange material on crevice corrosion of high-grade stainless steels (SS) and Ni-based alloys was studied by Larche et al. [25]. Here, the crevice corrosion performance of several SS and nickel alloys was evaluated at 30 °C and 50 °C in chlorinated and natural seawater for a three-month exposure time. Among the tested materials in this study are UNS N06022 and UNS S31266 which were found to be resistant to crevice corrosion under all experimental conditions. Gaskets are the crevice formers in flanged gasketed joints that are used to prevent leakage in these joints. The material of the

gasket is selected based on different factors, including the media inside the pipeline, temperature, pressure, bolting, and any cyclic or vibrational loading of the joint [26]. As gaskets are in direct contact with flanges in BFJ, their material affects crevice corrosion initiation and propagation on the flange surface [21]. This research mainly focuses on studying corrosion mechanisms on the flange face by changing the gasket material.

Various electrochemical techniques have been utilized in the literature to measure flange face corrosion. These methods were employed to assess the susceptibility of flange and gasket materials to crevice corrosion by comparing parameters such as the potential at which crevice corrosion initiates ( $E_{\text{crevice}}$ ) [20], the critical crevice temperature (CCT) at which crevice corrosion occurs [27], and the time required for crevice corrosion to initiate ( $t_{\text{init}}$ ) [24]. However, studies on the corrosion behavior of flange materials are typically conducted under conditions that are not representative of actual operating conditions. For instance, these studies are often performed under conditions without fluid circulation, the presence of a gasket, or sufficient gasket contact stress, despite the critical role these factors play in the initiation and growth of crevice corrosion [22].

In this paper, the developed Corrosion Quantification Test (COQT) rig and fixture by the authors, detailed in Ref. [28], are utilized to assess the impact of three types of gaskets: flexible graphite sheet, graphite sheet with foil inserts, and polytetrafluoroethylene (PTFE) sheet, on the corrosion behavior of ASTM A182 F321 flange material. This material is among the widely used SS flange materials [29]. The mentioned fixture takes into account both electrochemical attributes and service conditions, allowing for the quantification of corrosion behavior using three-electrode electrochemical techniques, including cyclic potentiodynamic polarization (CPP) tests and potentiostatic polarization tests. Employed in the current study, CPP is the most widely used technique for assessing critical crevice corrosion potentials, while potentiostatic tests provide information about the initiation and propagation of crevice corrosion [22].

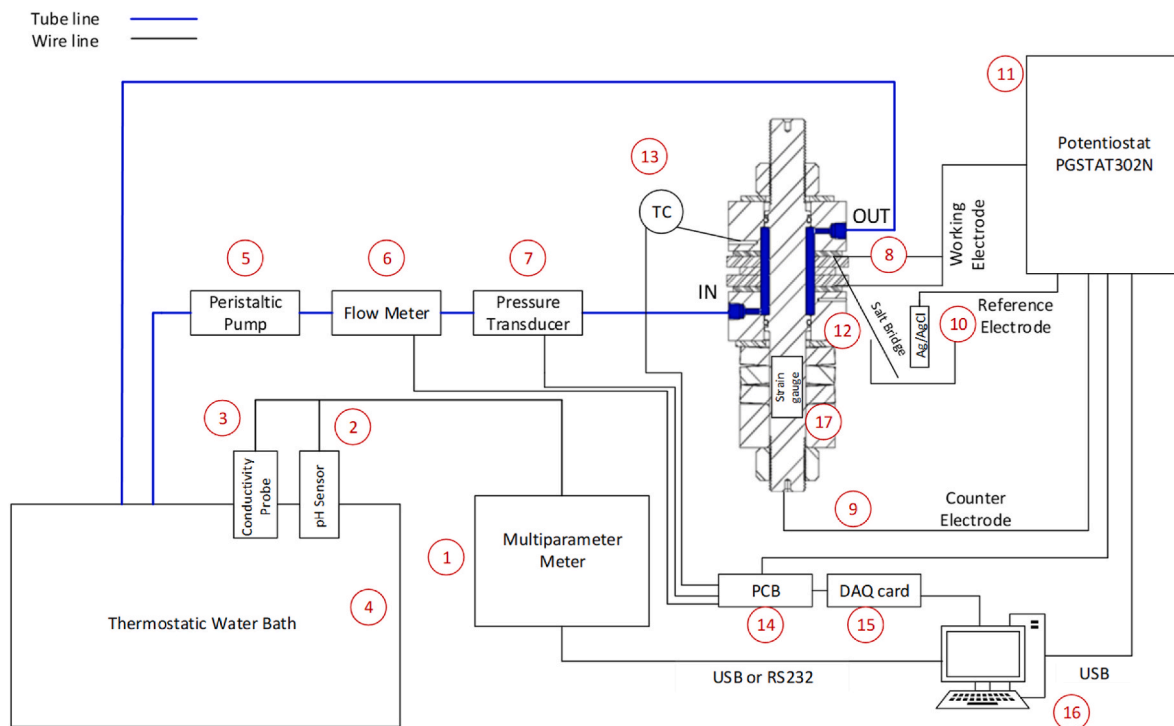


Fig. 2. COQT bench: 1) pH and conductivity meter; 2) pH electrode; 3) conductivity electrode; 4) thermostatic water bath; 5) peristaltic pump; 6) flow sensor; 7) pressure sensor; 8) working electrode connection; 9) auxiliary electrode connection; 10) reference electrode; 11) potentiostat; 12) salt bridge; 13) thermocouple; 14) PCB; 15) DAQ card; 16) PC; 17) strain gauge (adapted from Ref. [28]).

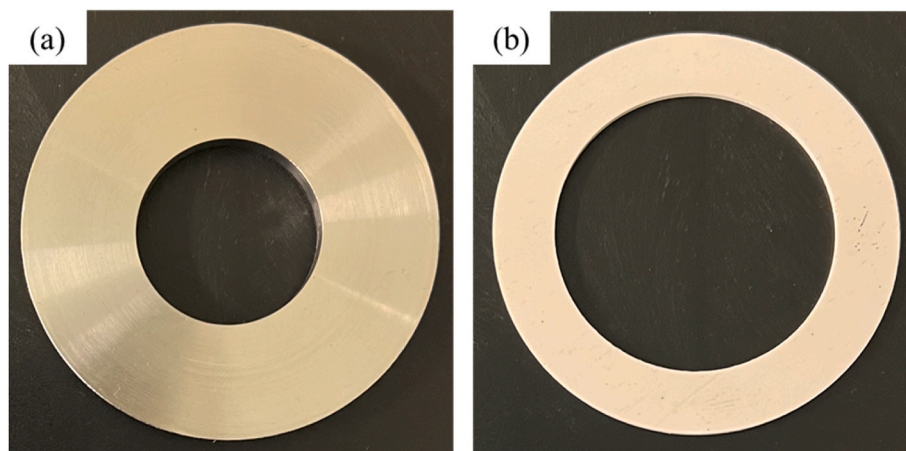


Fig. 3. An overview of (a) the 321 SS sample plate; (b) the virgin PTFE gasket.

## 2. Corrosion quantification test rig and fixture

### 2.1. Test fixture

The COQT test fixture, which is capable of measuring and analyzing the corrosion of sample plate and gasket material pairings, is depicted in Fig. 1. The fixtures' components are depicted in this image. It replicates the successful Aged Relaxation Leakage Adhesion (ARLA) device [30, 31], which measures weight loss, load retention, gasket relaxation, and leakage tightness after aging a sheet gasket material in an oven. The COQT fixture is designed to mimic ASME B16.5 [32], NPS 1½ class 150 (gasket according to ASME B16.21 [33] dimensions) BFJ. Through the use of a hydraulic tensioner, the central stud allows the application of compressive stress on the gasket through the circular compression plates. The slots on the compression plates are designed to quantify the difference in gasket thickness before and after the corrosion tests. The corrosive solution can also circulate through the entry and exit ports on the compression plates. The test fixture is meant to simulate a BFJ. After every test, it is simple to exchange the corroded sample plates for new ones in order to examine the effects of different factors. To precisely measure the corrosion of the sample plates and prevent corrosion of the rest of the fixture, the electrical insulator creates electrical insulation between the sample plates and the compression plates. The Belleville washer and compression plate have more surface area in contact when a plain washer is utilized. The Belleville washers help to keep the assembly's preload constant and, if necessary, to modify the bolt joint's stiffness. It should be mentioned that this parameter matters when taking relaxation into account. The Belleville washers have a robust contact interface due to the load ring or spacer. The O-rings provide a seal to the outside and stop the stud from making electrical contact with the plates. The plain washer increases the contact area between the compression plates and the nuts. The inside chamber has a 20 mL capacity. The gaskets size is within an ID of 1.31 inches and an OD of 2.95 inches with thicknesses ranging from 1/16" to 1/8".

### 2.2. Test rig

The COQT fixture is part of the test rig shown in Fig. 2. It is connected to a tank containing a corrosive solution with a ¼ inch diameter circuit that has different equipment and instrumentation. The multiparameter

meter (1) simultaneously measures the pH, conductivity, and temperature of the solution using a pH sensor (2) and a conductivity probe (3). The thermostatic water tank (4) is a container that heats the corrosive solution to the desired test temperature with precision of  $\pm 0.1$  °C. The peristaltic pump (5) provides continuous solution flow from the thermostatic water tank to the test fixture. The flow meter (6) and pressure transducer (7) continuously monitor the flow and pressure of the solution. The three-electrode system is used to quantify the corrosion according to ASTM G59 requirements [34]. Sample plates are considered as working electrodes (8), the central stud is considered as a counter electrode (9), and the Ag/AgCl as a reference electrode (10). In this test rig, the potentiostat (11) is the instrument that maintains the working electrode potential, and the measured potential is compared to the reference electrode. To reduce the ohmic drop contribution between the reference and working electrodes, the salt bridge (12) is utilized as a conductive connection between the solution in the test fixture and the reference electrode. The test fixture's temperature is determined by the thermocouple (13). The circulating solution soaks all internal components of the fixture, including the gasket and the metallic sample plates, as shown in Fig. 2, where it flows from the bottom to the top. The analogue signals from the sensors are transmitted to the printed circuit board (PCB-14) and converted to numerical values by the Data Acquisition Card (DAQ-15). The DAQ, potentiostat, and multiparameter meter are connected directly to the computer (16) through USB ports. A full Wheatstone strain gauge bridge is bonded to the central stud (transducer in mV) to measure the gasket load and converted to an average gasket contact stress (17).

## 3. Materials and methods

### 3.1. Materials

The sample plates, depicted in Fig. 3 (a), have an outer diameter of 2.95 inches, an inner diameter of 1.31 inches, and a thickness of 0.25 inches. The roughness of the sample plates was measured using a Mitutoyo profilometer following the ISO 21920-2:2021 standard, as recommended by literature [35]. A cut-off length of 0.8 mm and a short wavelength cut-off filter  $\lambda_s$  of 2.5  $\mu\text{m}$  were used, resulting in an arithmetic mean of absolute height values  $R_a = 1.006 \pm 0.05$   $\mu\text{m}$ . The material of the sample plate is 321 SS, which has a chemical composition

Table 1

Chemical composition of 321 SS sample plate (wt.%).

C	N	Si	P	S	Cr	Mn	Ni	Mo	Cu	Ti
0.049	0.024	0.54	0.03	0.001	17.45	1.57	9	0.37	0.48	0.53

**Table 2**  
Characteristics of G-1 and G-2 gaskets.

Gasket	Ash content (%)	Density (g/cm <sup>3</sup> )	Chloride content (ppm)	Fluorine content (ppm)	Sulfur content (ppm)	Total halogen (ppm)
G-1	≤2.0	1.1	≤50	≤10	≤750	≤310
G-2	≤2.0	1.1	≤25	≤10	<300	≤70

according to ASTM A182 [36] standard specification for SS pipe flanges. The chemical composition is provided in

Table 1. Between the sample plates, three types of gaskets including graphite sheet gasket (G-1), graphite gasket with metal foils (G-2), and virgin PTFE sheet gasket with dimensions of 1.92 inches inner diameter, 2.8 inches outer diameter, and 1/16-inch thickness are utilized (Fig. 3 (b)). Table 2 provides G-1 and G-2 gaskets characteristics. The PTFE samples are made of barium sulfate filled PTFE gasketing material.

### 3.2. Corrosion characterization

The current research uses electrochemical techniques and microscopic characterisation to explore the corrosion mechanism on the surfaces of the flanges in BFJs. These techniques will be discussed in the following sections.

#### 3.2.1. Cyclic potentiodynamic polarization

The CPP test (according to ASTM G61 [37]), is performed to measure the corrosion mass loss rate and quantify crevice corrosion behavior of flange materials. The three-electrode cell used for electrochemical measurements, including the sample flange plates (321 SS) as a working electrode (W.E.), a saturated Ag/AgCl as a reference electrode (R.E.), and 316L SS (central stud) as a counter electrode (C.E.). All potentials mentioned in this paper are measured with respect to the Ag/AgCl electrode, as the potential of this electrode does not change during the test. Before starting the polarization test, the fixture shown in Fig. 1 is mounted on a stand equipped with a hydraulic tensioner to compress the gasket to an average low stress level of 15 MPa to account for the service loads such hydrostatic end effect and relaxation due to creep that tend to unload the gasket. The maximum stress that can be applied to the gasket with this fixture is 35 MPa. This low stress level ensures a tight seal, while facilitating solution penetration into the small gaps and leak paths, which is ideal for evaluating the impact of gasket material on crevice corrosion propagation. It should be noted that the fixture is designed to allow low pressure of the saline solution and in all cases, it remains below 0.1 MPa. Given this low-pressure level and the fact that hydrostatic area is confined between the central stud shank OD and gasket ID, the contribution of the hydrostatic end force to the overall gasket stress is negligible. A one litre glass cell of 3.5 wt% NaCl solution (distilled water and analytical grade of NaCl) is placed in the thermostatic water bath and the temperature is set to  $22 \pm 1$  °C, then the peristaltic pump circulates the solution in the fixture with a flow rate of 20 mL/min. The polarization test is initiated 24 h after the solution has been in circulation inside the fixture, allowing sufficient time for the surfaces of the samples and the interface between the gaskets and sample plates to become wet. The scan begins from 0.03 V below the Open Circuit Potential (OCP) and continues until the current reaches 5 mA, at which point it is reversed. The scan is discontinued when the potential reaches 0.03 V. For both forward and reverse scan, the scan rate is 0.167 mV/s. The exposed surface area of the 321 SS sample plates is 33.28 cm<sup>2</sup>. Autolab potentio/galvanostat PGSTAT302N-High Performance is used to produce the polarization curves for the discussed potential ranges. Nova software version 2.1.6 is used to calculate  $i_{corr}$  according to Equation (1) for each polarization curve. Before polarization tests, the specimen plates are degreased with acetone followed by alcohol, and then air dried. To ensure result producibility, all polarization tests are conducted at least three times.

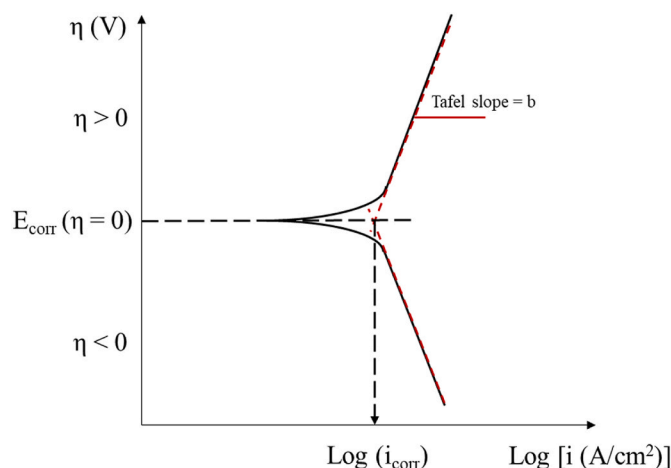


**Fig. 4.** A schematic overview of the Tafel extrapolation represents the corrosion potential ( $E_{corr}$ ), overpotential ( $\eta$ ), Tafel slope ( $b$ ), and corrosion current density ( $i_{corr}$ ).

#### 3.2.2. Electrochemical analysis method

Corrosion is an electrochemical reaction in which the electrons are reactants. Therefore, the rate of reactions is controlled by varying the potential. In polarization tests, the anodic or cathodic reaction rates are controlled by withdrawing or adding the electrons to the system, which is typically achieved by precisely controlling the potential using a potentiostat. The potential at which the cathodic and anodic reaction rates are equal is defined as the corrosion potential ( $E_{corr}$ ), and the related current density is defined as the corrosion current density ( $i_{corr}$ ). Tafel extrapolation is used to determine the corrosion current density. The Tafel equation shows the relation between the current density and potential according to Equation (1) [38].

$$E - E_{corr} = a \pm b \log|i| \quad (1)$$

here  $E$  is the applied potential in V,  $E_{corr}$  is the potential where corrosion occurs,  $E - E_{corr}$  is the overpotential ( $\eta$ ) in V, the sign " $\pm$ " indicates in which domain the sample operates (+ if anodic and - if cathodic),  $a$  and  $b$  are the Tafel constant and slope, respectively, and  $i$  is the current density in A/cm<sup>2</sup>. The current density is obtained by dividing the measured current to the geometric area of the working electrode exposed to the solution. Fig. 4 depicts the schematic overview of the Tafel extrapolation technique used to determine  $i_{corr}$  and  $E_{corr}$ . The intersection of the extrapolated Tafel anodic line ( $\eta > 0$ ) and the Tafel cathodic line ( $\eta < 0$ ) with  $E_{corr}$  determines  $i_{corr}$ , which provides the corrosion rate or mass loss rate. All the electrochemical parameters in Fig. 4 are defined in the explanation of Equation (1).

In situations where general corrosion occurs, Equation (2) converts the  $i_{corr}$  to the mass loss rate using Faraday's law. This mass loss rate indicates the general corrosion rate in grams per square meter per day (g/m<sup>2</sup>/d).

$$MR = Ki_{corr} EW \quad (2)$$

where  $MR$  is mass loss rate in g/m<sup>2</sup>/d,  $K$  is  $8.954 \times 10^{-3}$  gcm<sup>2</sup>/μA/m<sup>2</sup>/d,  $i_{corr}$  is in μA/cm<sup>2</sup>, and  $EW$  is the dimensionless equivalent weight.  $EW$  is the mass of metal oxidized by the passage of 1 F (96500C) of electric charge. The value of  $EW$  for typical stainless steel and carbon steel is provided in ASTM G102 [39].

#### 3.2.3. Potentiostatic polarization

Since the potentiodynamic test discussed in the previous section was destructive, new samples are employed for the potentiostatic tests. Following a 24-h period of 3.5 wt% NaCl solution circulation in the fixture, potentiostatic tests are conducted at three time intervals: 6, 12,

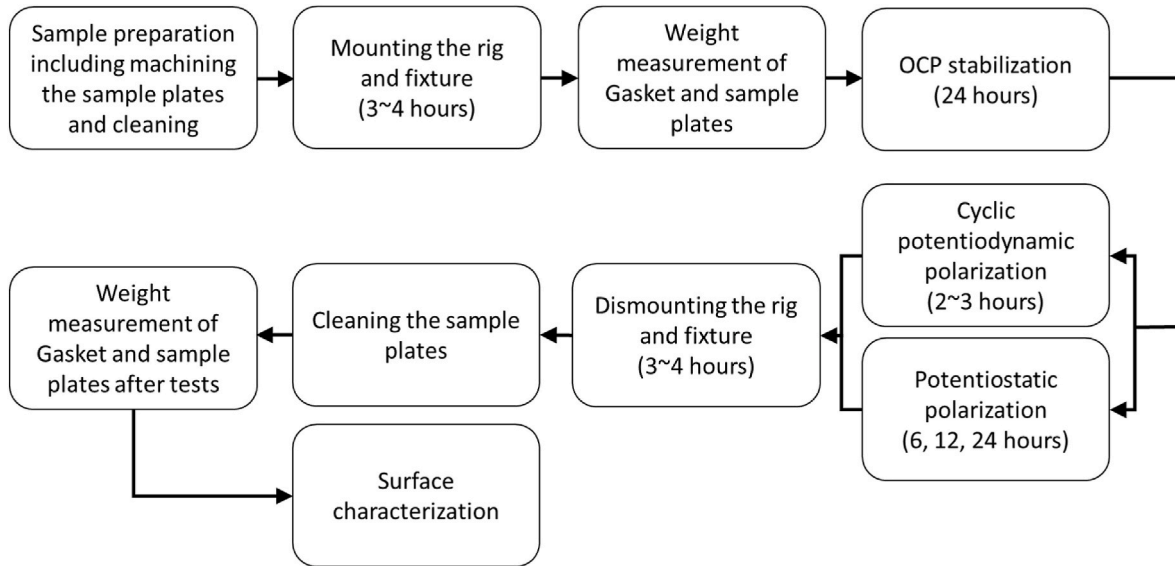


Fig. 5. Flowchart indicating the experimental methodology.

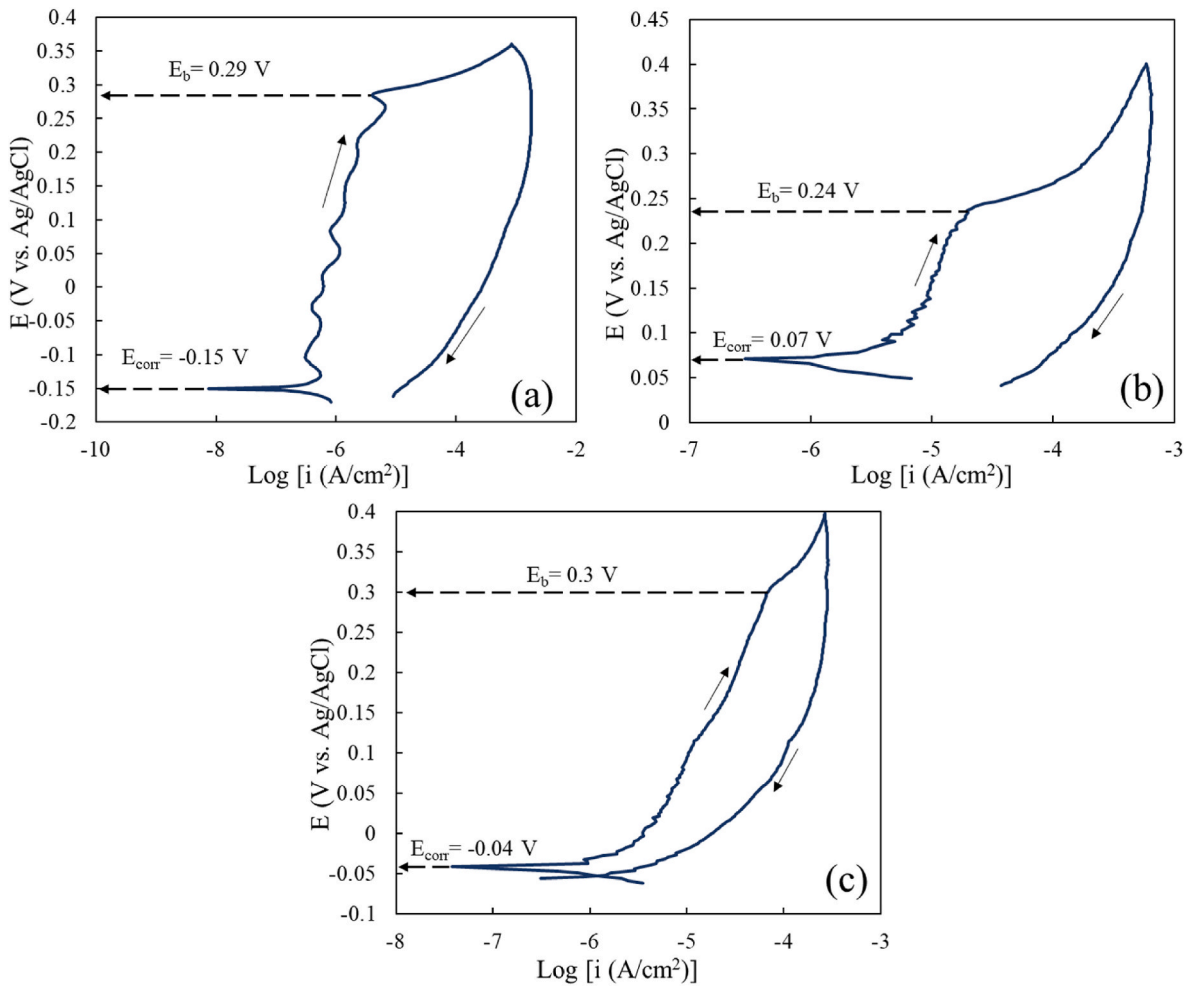


Fig. 6. Potentiodynamic polarization curves of 321 SS sample plates coupled with (a) PTFE gasket; (b) G-1 gasket; and (c) G-2 gasket at 15 MPa gasket contact stress in 3.5 % NaCl solution.

**Table 3**

Main electrochemical parameters obtained from the polarization curves.

Sample	$E_{corr}$ (V)	$E_b$ (V)	$ E_{corr} - E_b $ (V)	$i_{corr}$ ( $\mu\text{A}/\text{cm}^2$ )	MR ( $\text{g}/\text{m}^2/\text{d}$ )
321 SS and PTFE	-0.15	0.29	0.44	0.15	0.03
321 SS and G-1	0.07	0.24	0.17	0.59	0.13
321 SS and G-2	-0.04	0.3	0.34	0.28	0.06

and 24 h at  $0.15 V_{Ag/AgCl}$  for each gasket material.

### 3.3. Surface characterization

A Laser Confocal Microscope LEXT4100 is utilized to examine the surfaces of the corroded samples after the potentiostatic tests, enabling visualization of the damage caused by corrosion. This includes the examination and evaluation of crevice corrosion in terms of surface and depth. The corroded areas on the surface of the sample plates are measured using Fiji software, an open-source platform for image analysis [40]. The entire corroded surface area ( $A_c$ ) is calculated using Equation (3).

$$A_c = \sum_i^n A_{c,i} \quad (3)$$

where  $A_{c,i}$  represents the corroded area in region  $i$ , and  $n$  stands for the number of observed corroded areas on the sample plate surface. The morphology of the corroded area is analyzed using scanning electron microscopy (SEM). The Keyence VR-5200 digital microscope is used to examine the corroded surface of the sample plates, providing a zoomed-

out view to illustrate the propagation mechanism of crevice corrosion.

To summarize the developed methodology, Fig. 5 presents a flow-chart including the different experimental steps followed in this study.

## 4. Results

### 4.1. Cyclic potentiodynamic polarization curves

Fig. 6(a–c) displays the results of CPP for the 321 SS sample plates assembled with virgin PTFE gasket, G-1 gasket, and G-2 gasket, while subjected to identical gasket contact stress, fluid flow rate, and temperature (as mentioned in section 3.2.1). These polarization curves measure the corrosion potential ( $E_{corr}$ ) and breakdown potential ( $E_b$ ) to evaluate the corrosion behavior of the samples. The corrosion potential represents the potential of the working electrode (sample plate) in relation to the reference electrode when no potential or current is applied to the working electrode. It serves as a thermodynamic parameter indicating the tendency of the working electrode to engage in corrosion reactions under specific conditions. In  $E_b$ , the current density experiences a significant and rapid increase. A higher positive breakdown potential obtained at a fixed scan rate in the polarization curve indicates a reduced susceptibility of the sample plate to the onset of localized corrosion (crevice or pitting corrosion) [22,41]. To estimate the overall corrosion rate of the sample plates, the corrosion current density ( $i_{corr}$ ) is calculated for each polarization curve using the Tafel equation (Equation (1)). The difference between  $|E_{corr} - E_b|$  characterizes the inclination towards localized corrosion, with higher values signifying a reduction in tendency [42]. Table 3 provides an overview of the primary electrochemical parameters obtained from the polarization

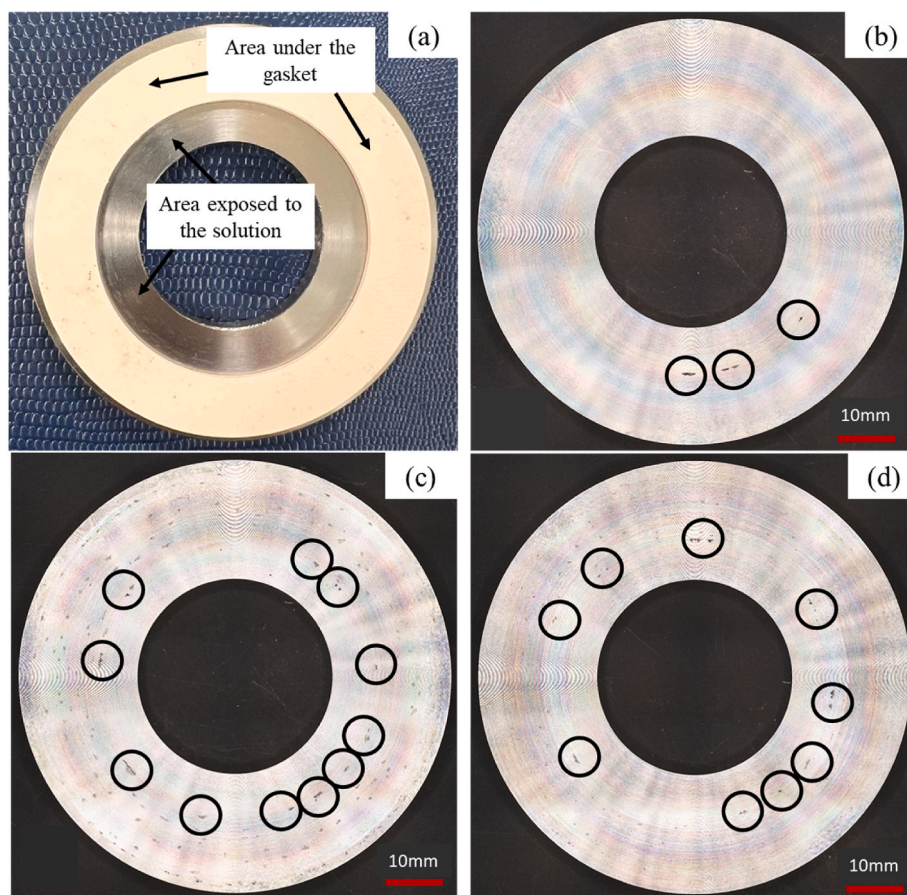


**Fig. 7.** 321 SS sample plates before and after corrosion tests; (a) Configuration of the gasket and 321 SS sample plate; (b) Crevice corroded area on the 321 SS sample plate with virgin PTFE gasket; (c) Crevice corroded area on the 321 SS sample plate with G-1 gasket; (d) Crevice corroded area on the 321 SS sample plate with G-2 gasket.

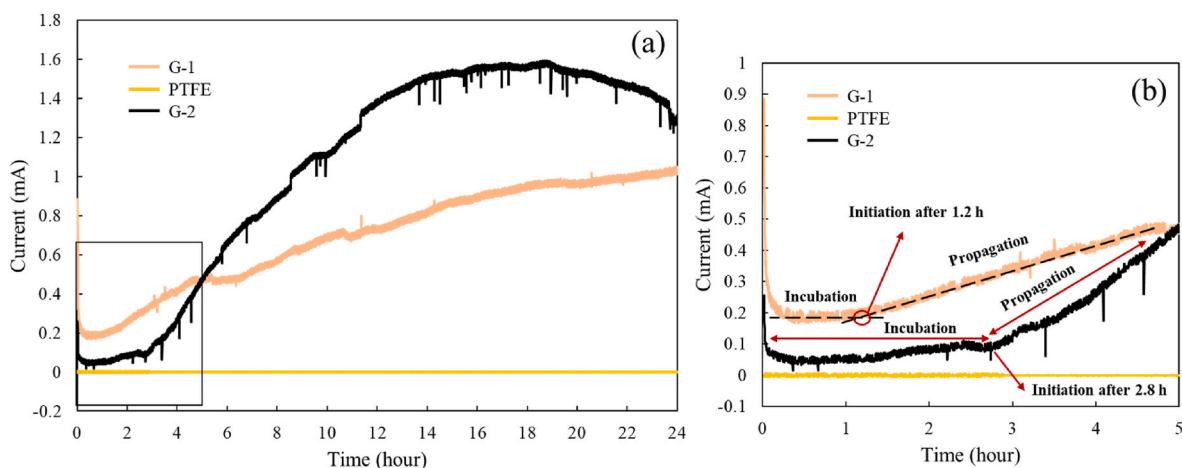


**Fig. 8.** Time-dependent of polarization current behavior of 321 SS sample plates under 0.15 V in 3.5 wt% NaCl solution with various gasket materials. a) the time-dependent polarization for 24 h; b) magnification of the initial 5 h of the polarization curve revealing distinct stages of crevice corrosion.

curves in Fig. 6. The  $E_{corr}$  value for the sample plate with the virgin PTFE gasket ( $-0.15$  V) is found to be lower compared to the other specimens. The  $E_{corr}$  of the 321 SS sample plates with a G-1 gasket (0.07 V) was observed to be higher than that of the specimen with a G-2 gasket ( $-0.04$  V). In terms of localize corrosion tendency, represented by the  $|E_{corr} - E_b|$  difference, the 321 SS specimens with the virgin PTFE gasket exhibited a higher potential difference (0.44 V) compared to the specimens with the G-1 gasket (0.17 V) and G-2 gasket (0.34 V). This indicates that the joint with the virgin PTFE gasket has the lowest tendency for localize corrosion. The presence of graphite causes a galvanic effect, leading to higher MRs for the specimens with G-1 (0.13  $\text{g}/\text{m}^2/\text{d}$ ) and G-2 (0.06  $\text{g}/\text{m}^2/\text{d}$ ) compared to the specimen with the PTFE gasket (0.03  $\text{g}/\text{m}^2/\text{d}$ ). According to the potentiodynamic polarization results, the galvanic effect between the graphite gaskets and 321 specimen plates leads to a higher corrosion rate compared to the specimens coupled with a PTFE gasket. With regard to the galvanic effect, graphite, having a higher potential than the 321 SS, acts as the cathode, while the 321 SS specimen serves as the anode, resulting in accelerated corrosion on the surface of the samples exposed to the solution [43,44].

As mentioned above,  $E_b$  is the potential at which the passive layer breaks down. This occurs due to pitting corrosion and/or crevice corrosion. Fig. 7 shows that the breakdown of the passive layer occurs at the sample plate-gasket interface. Therefore, in this case, the breakdown of the passive layer is attributed to crevice corrosion on the surface of the plates. The configuration of the gasket and sample plates are defined in Fig. 7 (a). Different areas on the sample plate surface are highlighted, including the area under the gasket and the area exposed to the solution. The crevice corroded 321 SS sample plate, after being coupled to PTFE gasket is shown in Fig. 7 (b). The image shows the corroded sites by circles, and the crevice corrosion is observed in the boundary of the area exposed to the solution and the area under the gasket. The corroded sample plates of Fig. 7 (c) and (d) are associated to the G-1 and G-2 gaskets, respectively. The corroded sites in the boundary of the exposed area and the area under the gasket are shown with circles. Additionally, corroded sites under the gasket area, are observed with graphite gaskets but not with virgin PTFE gaskets.

#### 4.2. Potentiostatic polarization test and surface analysis

The potential at which potentiostatic polarization is conducted is adjusted such that it falls within the passivation region, as indicated by the polarization curves in Fig. 6. Fig. 8 (a) depicts potentiostatic polarization curves of 321 SS plates in a 3.5 % NaCl solution using the three gasket materials over a 24-h period. The crevice corrosion is divided to three stages based on the polarization curve features: 1) incubation, 2)

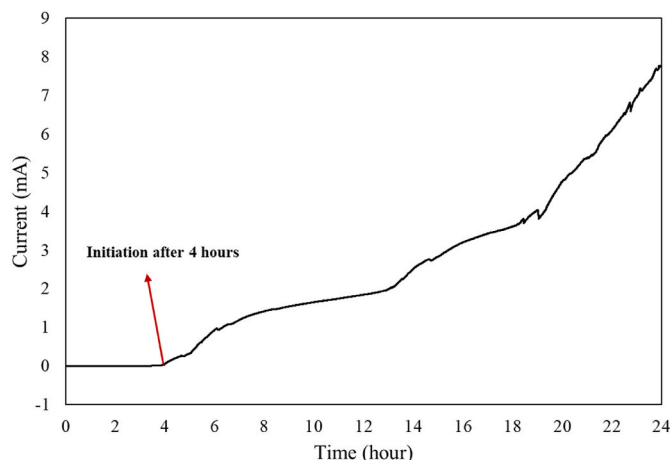


**Fig. 9.** Time-dependent of polarization current behavior of 321 SS sample plates under 0.3 V in 3.5 wt% NaCl solution with virgin PTFE gasket.

initiation, and 3) propagation. These stages are marked in Fig. 8 (b). The results indicate that the initiation time for the sample plate with the G-1 gasket is 1.2 h, while for the sample plate with the G-2 gasket, it is 2.8 h. In the case of the sample plate with the PTFE gasket, crevice corrosion did not initiate. To investigate the crevice corrosion propagation in the sample plate with PTFE gasket, the potentiostatic test is performed at a higher potential of 0.3 V. As depicted in Fig. 9, the initiation time for the sample with the PTFE gasket is 4 h. This indicates that even at higher potentials, it takes more time for crevice corrosion to initiate compared to G-1 and G-2. The potentiostatic tests indicate that the sample coupled with the G-1 gasket is more susceptible to crevice corrosion initiation, which is in accordance with the potentiodynamic polarization test results.

To investigate the corrosion morphology on the surface of the corroded sample plates, surface analysis was conducted after 24 h of potentiostatic tests, as depicted in Fig. 10. As indicated in Fig. 10 (a) and (b), corrosion took place not only along the boundary of the area exposed to the solution but also beneath the G-1 gasket. In fact, corrosion extended beyond the gasket immediate boundary. For the corroded sample plate used with the G-2 gasket, Fig. 10 (c) and (d) reveal that corrosion was mainly concentrated along the boundary of the exposed area, forming a distinct ring. In contrast, the corroded area on the sample plate coupled with the PTFE gasket appeared to be deeper than the others. Corrosion occurred along the boundary of the exposed area

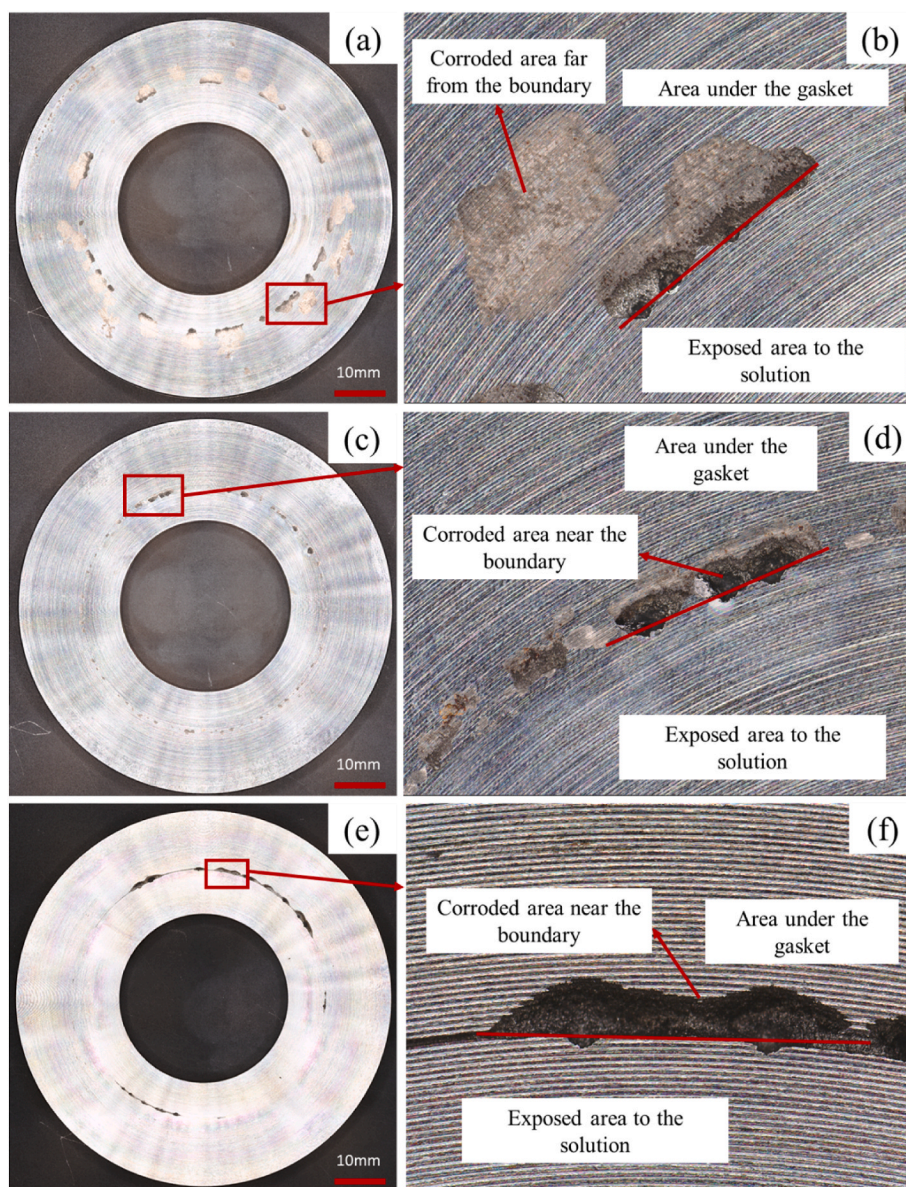


**Fig. 10.** Morphology of the crevice corrosion after potentiostatic test of 321 SS sample plates with different gasket material. a) Crevice corrosion on the sample plate with G-1 gasket at 0.15 V; b) magnified image of the corroded sample plate used with G-1 gasket with specified area; c) crevice corrosion on the sample plate with G-2 gasket at 0.15 V; d) magnified image of the corroded sample plate used with G-2 gasket with specified area; e) crevice corrosion on the sample plate with PTFE gasket at 0.3 V; f) magnified image of the corroded sample plate used with PTFE gasket with specified area.

and under the gasket, but it did not encircle the entire boundary. Instead, deep corrosion spots were observed, as illustrated in Fig. 10 (e) and (f).

For further examination, the corroded sites are examined after 6 h of potentiostatic test using the confocal microscope, and the deepest corroded sites are magnified. Fig. 11 (a) indicates the 3D surface morphology of a single crevice corrosion occurred on the sample plate coupled with G-1 gasket. The graphical representation of the corrosion damage depth profile along the cross-section line (indicated in Fig. 11 (a)) of the single crevice site is shown in Fig. 11 (b). The region that is covered by the gasket during the corrosion tests is schematically shown in this figure. The corrosion profile has a maximum depth of the 28  $\mu\text{m}$  in the severely attacked region. The same approach is done for the 321 SS sample plates with PTFE and G-2 gaskets. Fig. 11 (c) shows the magnified corroded site of the sample plate, and the depth of the severely corroded area is measured in Fig. 11 (d) which is 108  $\mu\text{m}$ . Fig. 11 (e) indicates the magnified 3D morphology of the crevice corrosion on the

sample plate with G-2 gasket. The depth of the deepest corroded site is measured as 72  $\mu\text{m}$  in Fig. 11 (d).

On the corroded surfaces, there are three distinct regions that can be observed, stretching from the boundary between the exposed area and the area under the gasket to the interior of the crevice. These regions are referred to as the passive region, severely attacked region, and lightly attacked region. The passive region represents the least affected area, encompassing the entirety of the exposed area on the plates. The severely attacked region begins at the edge of the area under the gasket, also known as the passive-to-active boundary. The lightly attacked region experiences less corrosion compared to the severely attacked region, primarily due to restricted diffusion of the solution into this area.

To investigate the corrosion growth mechanism at the interface of the gasket and sample plate, the corroded regions on the sample plate surfaces at three-time intervals are examined: 6, 12, and 24 h after initiating potentiostatic tests. The corroded area on the surface and the deepest corroded spot on the sample plates are quantified, with the

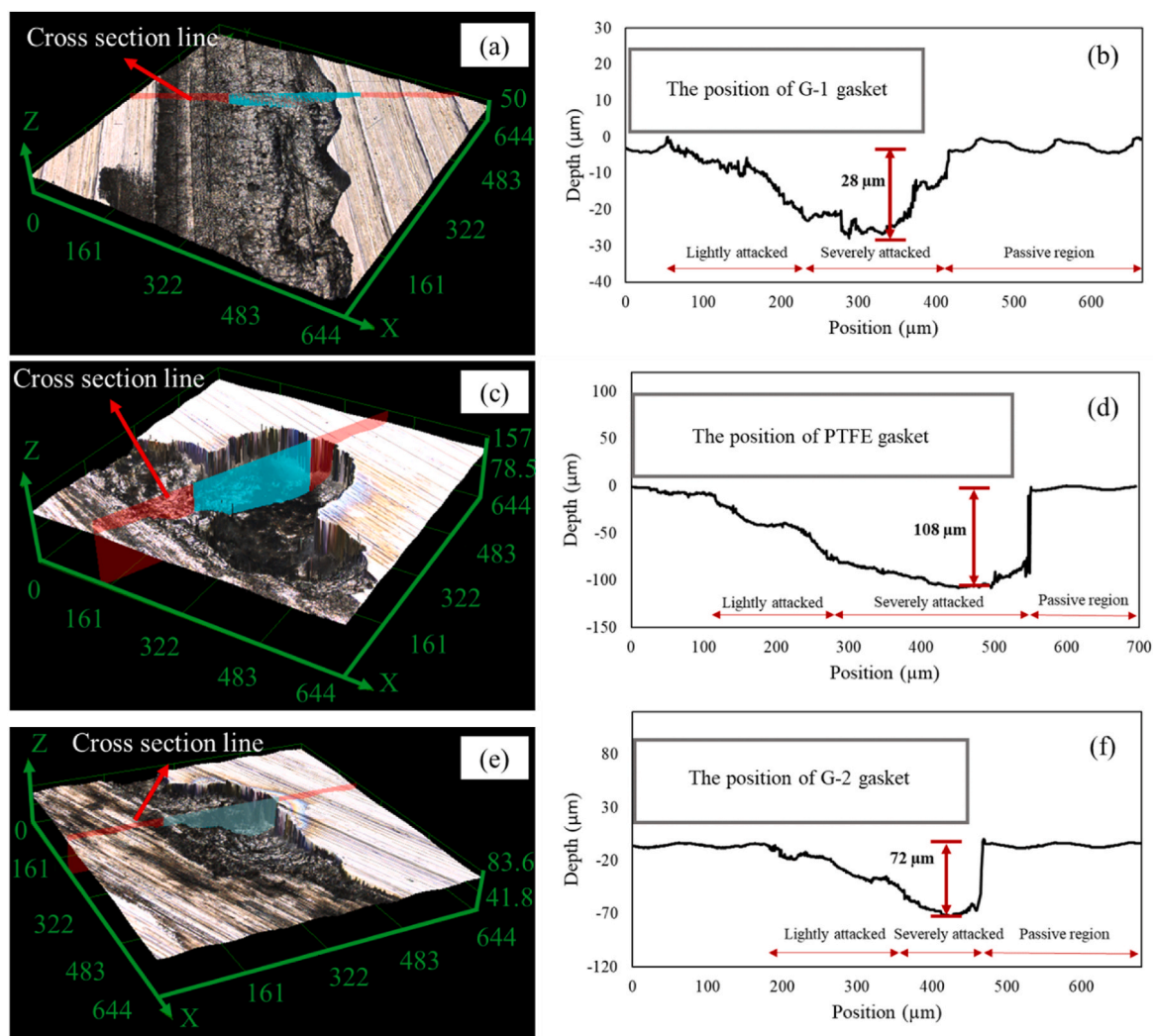


**Fig. 11.** Magnified crevice corroded site on the 321 SS samples used in joint with gaskets; (a) 3D surface morphology on a single crevice corrosion site for the 321 SS samples used with G-1 gasket; (b) graphical representation of a single crevice corrosion profile for the 321 SS sample used with G-1 gasket; (c) 3D surface morphology of a single crevice corrosion site for the 321 SS sample used with virgin PTFE gasket; (d) graphical representation of a single crevice corrosion profile for the 321 SS sample used with virgin PTFE gasket; (e) 3D surface morphology of a single crevice corrosion site for the 321 SS sample used with G-2 gasket; (f) graphical representation of a single crevice corrosion profile for the 321 SS sample used with G-2 gasket.

results presented in Fig. 12 (a) displays the deepest corroded regions on the surface of the 321 SS sample plates coupled with three different gaskets. Over time, the depth of the deepest corroded region increased for the sample plates with all three gaskets. Notably, the deepest corroded region was most pronounced for the sample plate coupled with the PTFE gasket, surpassing the others. In terms of the depth of the deepest corroded region, the ranking across the three-time intervals is as follows: PTFE > G-2 > G-1.

Fig. 12 (b) illustrates that the corroded area on the sample plate surfaces expanded over time for all three gaskets. The corroded area on the G-1 gasket is significantly larger than that on the others, while the corroded areas on the sample plates used with G-2 and PTFE gaskets exhibited similar growth trends. The order of corroded area size is as follows: G-1 > G-2 > PTFE.

#### 4.3. Gasket weight increase

After conducting potentiostatic polarization tests, the weights of the gaskets are compared to their initial values before testing, and the increased values are recorded in Table 4. The weight of the gaskets increased due to the absorption of the test solution by the gasket materials. Among the gaskets, the G-1 gasket exhibited the highest

absorption with a weight increase of 419 mg, followed by the G-2 gasket with a weight increment of 105 mg, and the PTFE gasket with a weight increase of 1.3 mg. Additionally, the thickness of the gaskets after applying a compression load are measured and reported in Table 4. As mentioned in section 3.1, all gasket types in this study initially have a thickness of 1/16 in (1.58 mm). However, when subjected to the same compressive load, the G-1 gasket compressed more than the others, resulting in a compressed thickness of 1.04 mm. The G-2 and PTFE gaskets have compressed thicknesses of 1.14 mm and 1.47 mm, respectively. The thickness of the gasket in the joint has an inverse relationship with the susceptibility of the 321 SS sample plates to crevice corrosion. As the joint thickness decreases, the diffusion of the solution to the gap between the two plates is restricted. This restricted diffusion leads to the acidification of the stagnant solution in the gap, intensifying crevice corrosion [45,46].

#### 4.4. Corrosion morphology

The initiation of crevice corrosion on the surface of the 321 SS sample plates occurs at a distance near the gasket, as shown in Fig. 13 (a). The corroded area near the gasket serves as a pathway for the corrosive solution to diffuse into the region between the plate and the

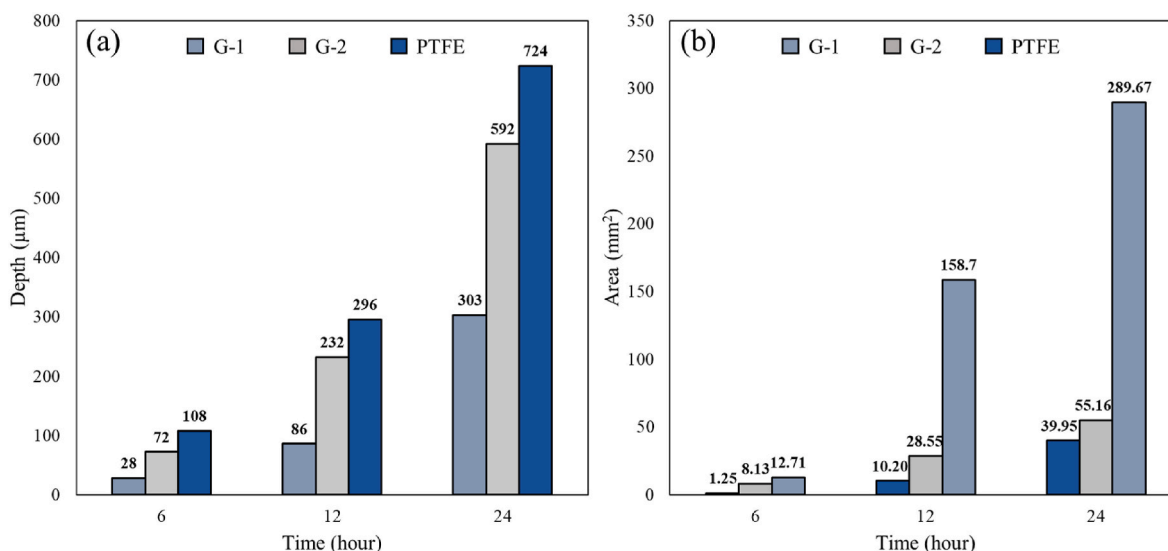


**Fig. 12.** Results of measurement of the (a) penetration depth and (b) corroded area of the 321 SS sample plates over time following potentiostatic tests with various gasket materials.

**Table 4**

Gasket characteristic after 24 h potentiostatic tests.

Type of gasket	Weight increase (mg)	Thickness after applying compressive load (mm)
G-1	419	1.04
G-2	105	1.14
PTFE	1.3	1.47

gasket, leading to the propagation of crevice corrosion within the crevice itself (area under the gasket), as depicted in Fig. 13 (b) and (c). In the lightly corroded area (Fig. 13 (d)), elongated pits and micro-cracks are observed, ranging in length from 5 to 40 µm. Furthermore, micro-pits are found surrounding the propagation front (Fig. 13 (e)), indicating a potential role of pits coarsening process in controlling the crevice propagation. Additionally, micro-cracks are observed within the micro-pits, possibly attributed to applied stress causing the widening of the pits. The pits that are observed in other reference are without cracks in compared to the pits observed in this study [47–49].

## 5. Discussion

### 5.1. Crevice corrosion initiation

Based on the results obtained from electrochemical tests, surface analysis, and measurements of gasket geometry and weight, the primary factor influencing the corrosion behavior of the 321 SS sample plates is the type of gasket material and its geometry. According to the findings from the CPP tests in section 4.1, it is evident that the 321 SS sample plates used with the G-1 gasket exhibit a higher susceptibility to crevice corrosion compared to the other types. Similarly, the potentiostatic tests conducted in section 4.2 indicate that the crevice corrosion initiation time for samples used with the G-1 gasket is shorter than for the other two gaskets. Furthermore, the initiation time for samples used with the G-2 gasket was shorter than for those used with the PTFE gasket. The variation in gasket thickness after applying the same amount of load appears to be the key contributing factor to differences in crevice corrosion susceptibility. As highlighted in Table 4, the G-1 gasket exhibits the lowest thickness after applying the same amount of load among all the gaskets. The lower thickness of the G-1 gasket, results in the formation of a stagnant solution near the gasket inside diameter. The same rationale explains the higher susceptibility of the G-2 gasket

compared to the PTFE gasket. The thickness of the gasket determines the gap between the two flanges which is the dominant factor in the initiation mechanism of the crevice corrosion [45]. Conversely, the thickness of the G-2 and PTFE gaskets is greater, leading to a delayed initiation of crevice corrosion in the samples with the G-2 gasket and no initiation in the samples with the PTFE gasket when a voltage of 0.15 V is applied.

The initiation of crevice corrosion can be explained by the potential drop (IR drop) theory [50], i.e., the decrease in potential that occurs within a crevice or gap as a result of the resistance encountered by an electric current passing through the solution in the crevice, which states that when the surface of the SS is in the passive form, the IR drop causes the crevice area to transition into the active region, initiating crevice corrosion. According to the IR drop theory, the ohmic potential drop is dependent on parameters such as current, solution conductivity, and crevice geometry. The value of this ohmic drop can be calculated using Eq. (4) [51,52]:

$$IR = \frac{x_{pass} I}{\sigma w t} \quad (4)$$

here,  $IR$  represents the potential drop in mV,  $x_{pass}$  is the distance between the crevice mouth and the active-passive boundary inside the crevice in cm,  $I$  is the current in mA,  $\sigma$  is the conductivity in  $\Omega^{-1} \text{cm}^{-1}$ ,  $w$  is the crevice width in cm, and  $t$  is the crevice gap thickness in cm. According to Eq. (4), the crevice gap thickness, which in this study is equal to the thickness of the gasket after applying the defined load, influences the IR drop and has an inverse relation. When the crevice gap thickness is high, as in the case of a PTFE gasket, the IR drop remains in the passive region, preventing the initiation of crevice corrosion.

### 5.2. Crevice corrosion propagation

As indicated in Table 4, G-1 absorbed a greater amount of solution compared to G-2 and PTFE gaskets. The surface analysis of the corroded samples at three different time intervals, as presented in Figs. 10 and 12, reveals distinct patterns of corrosion propagation based on the gasket type. In the sample plate used with the G-1 gasket, corrosion primarily occurred along the contact surface between the gasket and flange interfaces. This phenomenon can be attributed to the radial penetration of solution from inside to the outside of the G-1 gasket, as evidenced by the observed increase in weight. Conversely, for the G-2 gasket, which has a metal insert, water penetration was reduced, leading to corrosion primarily advancing in the depth of the sample. In the case of the PTFE

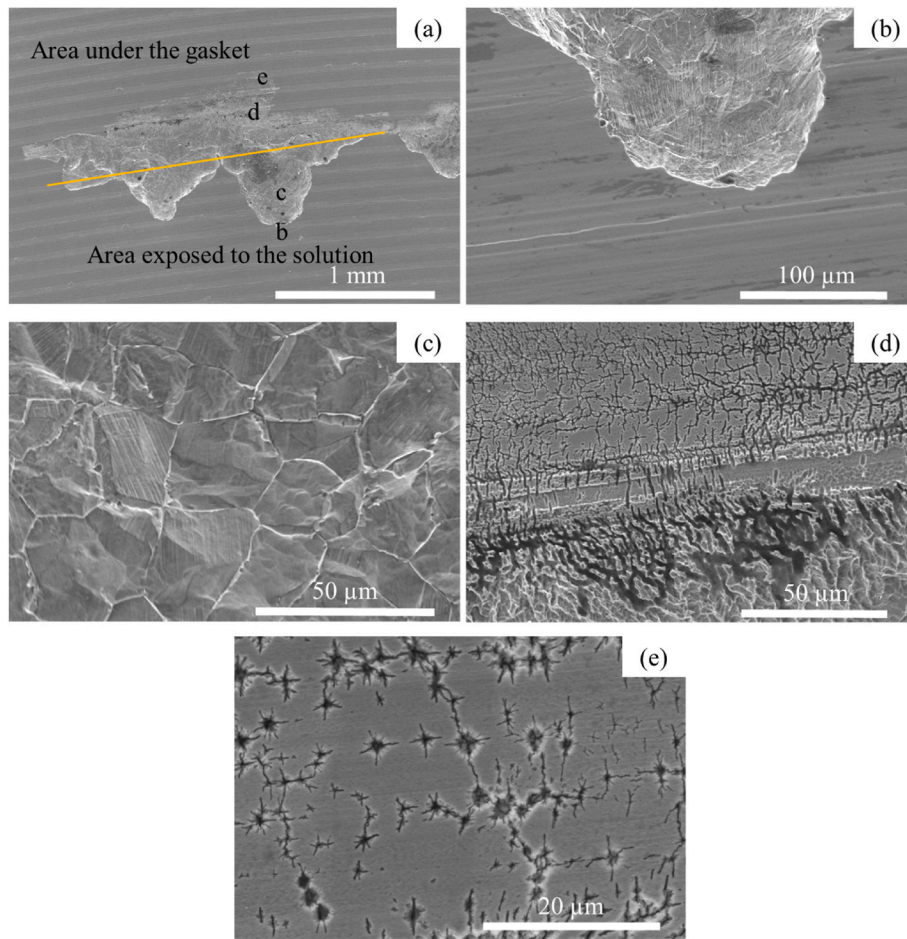


Fig. 13. SEM micrographs of different regions of the 321 SS sample plate coupled with G-1 gasket crevice corrosion; (a) the crevice corroded site; (b) boundary of the passive region and severely corroded region; (c) severely corroded region; (d) lightly corroded region; (e) pits near the lightly corroded region.

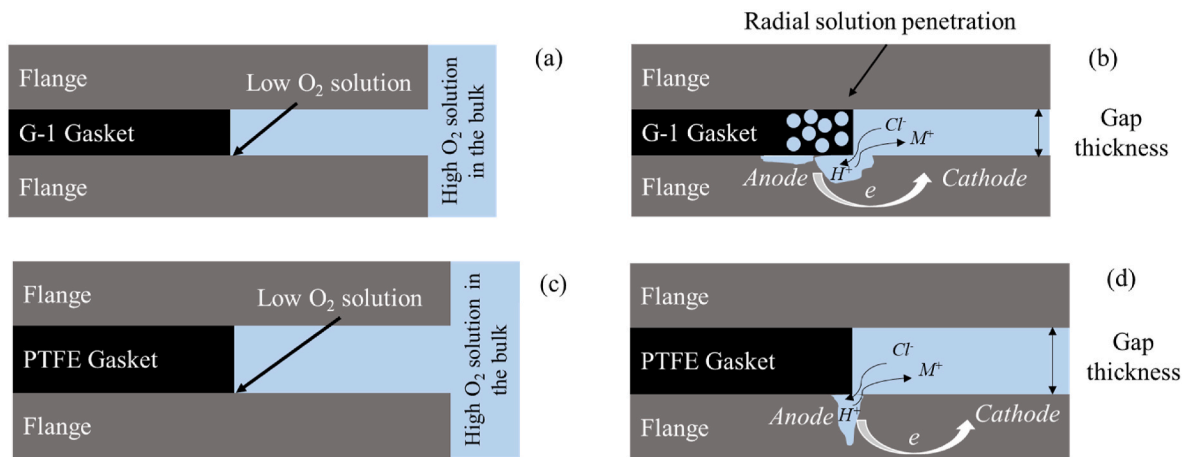


Fig. 14. Schematic overview of the mechanism of crevice corrosion in BFJs: a) a flanged joint with a G-1 gasket at the initial time of exposure; b) a flanged joint with a G-1 gasket after crevice corrosion initiation; c) a flanged joint with a PTFE gasket at the initial time of exposure; d) a flanged joint with a PTFE gasket after crevice corrosion initiation.

gasket, characterized by its hydrophobic nature [53], water penetration was negligible, resulting in corrosion predominantly progressing within the depth of the sample plate. Fig. 11 illustrates that the corrosion site near the gasket boundary acts as a pathway for the solution to diffuse into the crevice created at the interface of the gasket and specimen plate.

### 5.3. Mechanism of the corrosion

The mechanism of crevice corrosion in BFJs can be described as follows:

- 1) Crevice corrosion is significantly influenced by the occluded geometry of the crevice, restricting the mass transport of species into and out of the occluded region. In BFJs, the crevice is formed near the gasket inside diameter due to stagnation of the solution at the gap between the two flanges. Fig. 14 (a) and (c) present a schematic representation of the occluded solution in the gap in a BFJ with a gasket. According to the critical crevice solution theory [22,50], the solution becomes acidified due to the depletion of oxygen (O<sub>2</sub>) in the gap.
- 2) The reaction of metallic ions with chloride ions (Cl<sup>-</sup>) occurs, followed by the subsequent hydrolysis of metal chloride in water. This hydrolysis produces hydrochloric acid (HCl), reducing the pH in the gap to 2 [54]. The acidified solution then corrodes the 321 SS plate near the gasket, as shown in Fig. 14 (b) and (d). Subsequently, the acidified solution diffuses to the area between the gasket and the 321 SS specimen plate, leading to leakage over longer exposure times. For the 321 SS flange used with the G-1 gasket, the solution radially penetrates and causes a larger area of corrosion on the surface of the flange.

## 6. Conclusion

The comparison of polarization results, surface analysis, as well as gasket geometry and weight characterization revealed that:

- Two factors significantly influence corrosion at the interface of the flange and gasket: the size of the gap between the two flange surfaces and solution penetration into the gasket. These factors contribute to increased susceptibility to corrosion in joints used with graphite gasket materials compared to the PTFE gasket materials.
- Additionally, among the two graphite gaskets, the graphite sheet gasket (G-1) exhibits greater susceptibility to crevice corrosion than the graphite gasket with a metal insert (G-2) due to the formation of tighter gaps and a larger amount of solution absorption in the gasket structure.
- A larger corrosion area on the surface of the flange between the gasket and flange for the flange samples is obtained with the G-1 gasket causing corrosion propagation through the surface that eventually leads to early leakage comparatively with other gaskets.
- The corrosion propagation for the PTFE gasket was mainly through the depth of the flange near the gasket inside diameter; and therefore, would take more time for leakage to occur.

## CRedit authorship contribution statement

**Soroosh Hakimian:** Conceptualization, Formal analysis, Investigation, Methodology, Software, Validation, Visualization, Writing – original draft. **Abdel-Hakim Bouzid:** Methodology, Project administration, Resources, Supervision, Writing – review & editing, Funding acquisition. **Lucas A. Hof:** Funding acquisition, Methodology, Project administration, Resources, Supervision, Writing – review & editing.

## Declaration of competing interest

The authors declare that they have no known competing financial interests or personal relationships that could have appeared to influence the work reported in this paper.

## Data availability

Data will be made available on request.

## Acknowledgments

This work was supported by the Natural Sciences and Engineering Research Council of Canada (NSERC) under the Discovery Grant

(RGPIN-2019-05973 and RGPIN-2021-03780).

## References

- [1] A. Nechache, A.H. Bouzid, Creep analysis of bolted flange joints, *Int. J. Pres. Ves. Pip.* 84 (2007) 185–194, <https://doi.org/10.1016/J.IJPVP.2006.06.004>.
- [2] M. Abid, D.H. Nash, S. Javed, H.A. Wajid, Performance of a gasketed joint under bolt up and combined pressure, axial and thermal loading – FEA study, *Int. J. Pres. Ves. Pip.* 168 (2018) 166–173, <https://doi.org/10.1016/j.ijpvp.2018.10.014>.
- [3] K. Habib, Failure analysis of cracked reducer flange, *J. Fail. Anal. Prev.* 10 (2010) 480–485, <https://doi.org/10.1007/S11668-010-9389-9/FIGURES/14>.
- [4] X. Diao, Z. Chi, J. Jiang, A. Mebarki, L. Ni, Z. Wang, Y. Hao, Leak detection and location of flanged pipes: an integrated approach of principle component analysis and guided wave mode, *Saf. Sci.* 129 (2020) 104809, <https://doi.org/10.1016/j.ssci.2020.104809>.
- [5] S. Hakimian, A.-H. Bouzid, L.A. Hof, Corrosion failures of flanged gasketed joints: a review, *Journal of Advanced Joining Processes* 9 (2024) 100200, <https://doi.org/10.1016/J.JAJP.2024.100200>.
- [6] Y. Long, J. Luo, M. Yue, G. Wu, M. Zhao, N. Ji, W. Song, Q. Jin, X. Kuang, Y. Fan, Investigation on leakage cause of 13Cr pipe flange used for a Christmas tree in a high-pressure and high-temperature gas well, *Eng. Fail. Anal.* 142 (2022) 106793, <https://doi.org/10.1016/J.ENGFAILANAL.2022.106793>.
- [7] A. Nechache, A.H. Bouzid, On the use of plate theory to evaluate the load relaxation in bolted flanged joints subjected to creep, *Int. J. Pres. Ves. Pip.* 85 (2008) 486–497, <https://doi.org/10.1016/J.IJPVP.2008.01.005>.
- [8] A. Bouzid, A. Chaaban, A. Bazergui, The effect of gasket creep-relaxation on the leakage tightness of bolted flanged joints, *J. Pressure Vessel Technol.* 117 (1995) 71–78, <https://doi.org/10.1115/1.2842093>.
- [9] A. Bouzid, A. Chaaban, A. Bazergui, The influence of the flange rotation on the leakage performance of bolted flanged joints, in: *Canadian Society for Mechanical Engineering, QC, Montréal, 1994*.
- [10] A.H. Bouzid, M. Derenne, M. El-Rich, Y. Birembaut, Effect of Flange Rotation and Gasket Width on the Leakage Behavior of Bolted Flanged Joints, *Welding Research Council Bulletin*, 2004.
- [11] K. Worden, Flange corrosion: prevention and mitigation through better gasketing, *Fuels and Petrochemicals Division 2014 - Core Programming Area at the 2014 AIChE Spring Meeting and 10th Global Congress on Process Safety 2 (2014) 1000–1008*.
- [12] D. Nurhadyanto, Influence of Surface Roughness on Leakage of the Corrugated Metal Gasket, Yamaguchi University, 2014.
- [13] M. Bengtsson, Investigation of Galvanic Corrosion between Graphite Gaskets and Stainless Steel Flanges, Uppsala University, 2015.
- [14] A.P. Kölblinger, S.S.M. Tavares, C.A. Della Rovere, A.R. Pimenta, Failure analysis of a flange of superduplex stainless steel by preferential corrosion of ferrite phase, *Eng. Fail. Anal.* 134 (2022) 106098, <https://doi.org/10.1016/J.ENGFAILANAL.2022.106098>.
- [15] S. Al-Abbadi, H. Aoudi, W. AlShouly, W. Saeed, K. AlSafatli, A. Toubar, Crevice corrosion effect on alloy 625 in untreated seawater environment. *Society of Petroleum Engineers - SPE Abu Dhabi International Petroleum Exhibition and Conference 2017 2017-January, 2017*, <https://doi.org/10.2118/188302-MS>.
- [16] Q. Hu, Y. Liu, T. Zhang, F. Wang, Corrosion failure analysis on the copper alloy flange by experimental and numerical simulation, *Eng. Fail. Anal.* 109 (2020) 104276, <https://doi.org/10.1016/J.ENGFAILANAL.2019.104276>.
- [17] R. Francis, G. Byrne, Factors affecting gasket selection for stainless steels in seawater, in: *CORROSION 2007, Nashville, Tennessee, 2007*.
- [18] S.S.M. Tavares, J.M. Pardal, B.B. Almeida, M.T. Mendes, J.L.F. Freire, A.C. Vidal, Failure of superduplex stainless steel flange due to inadequate microstructure and fabrication process, *Eng. Fail. Anal.* 84 (2018) 1–10, <https://doi.org/10.1016/J.ENGFAILANAL.2017.10.007>.
- [19] S. Hakimian, A.-H. Bouzid, L.A. Hof, Effect of gap size on flange face corrosion, *Mater. Corros.* (2024), <https://doi.org/10.1002/MACO.202414367>.
- [20] Troels Mathiesen, Henrik Bang, Accelerated crevice corrosion testing of 6Mo stainless steel flanges with different gasket materials in seawater, in: *EUROCORR 2011, 2011, Stockholm*.
- [21] R.M. Kain, Gasket materials and other factors influencing the crevice corrosion resistance of stainless steel flanges, *Corrosion* 98 (1998). San Diego, California.
- [22] E.M. Costa, B.A. Dedavid, C.A. Santos, N.F. Lopes, C. Fraccaro, T. Pagartanidis, L. P. Lovatto, Crevice corrosion on stainless steels in oil and gas industry: a review of techniques for evaluation, critical environmental factors and dissolved oxygen, *Eng. Fail. Anal.* 144 (2023) 106955, <https://doi.org/10.1016/J.ENGFAILANAL.2022.106955>.
- [23] S. Hakimian, S. Pourrahimi, A.-H. Bouzid, L.A. Hof, Application of machine learning for the classification of corrosion behavior in different environments for material selection of stainless steels, *Comput. Mater. Sci.* 228 (2023) 112352, <https://doi.org/10.1016/J.COMMATSCI.2023.112352>.
- [24] Farrel J. Martin, Paul M. Natishan, Steven H. Lawrence, Elizabeth A. Hogan, Keith E. Lucas, Elvin Dail Thomas, Fluoroelastomeric gasket peculiarities influence the seawater crevice corrosion susceptibility of NiCrMo alloys, in: *CORROSION 2004, New Orleans, Louisiana, 2004*.
- [25] Nicolas Larché, Dominique Thierry, Pauline Boillot, Thierry Cassagne, Jérôme Blanc, Philippe Dézerville, Elisabeth Johansson, Jean Marc Lardon, Crevice corrosion performance of high grade stainless steels and Ni-based alloys in natural and treated seawater, in: *CORROSION 2016, Vancouver, British Columbia, 2016*.
- [26] Stephen Bond, Li Yi, A novel gasket design for an isolating gasket to solve common sealing problems, in: *CORROSION 2020, Virtual, 2020*.

- [27] Trond Rogne, John M. Drugli, Tone Solem, Hakon Salbu, Helge Sjljellevik, Crevice corrosion properties of weld overlays of Ni-based alloys compared to 6Mo stainless steels for seawater applications, *Corrosion* 98 (1998). San Diego, California.
- [28] S. Hakimian, A.H. Bouzid, L.A. Hof, An improved fixture to quantify corrosion in bolted flanged gasketed joints, *Journal of Pressure Vessel Technology, Transactions of the ASME* 146 (2024), <https://doi.org/10.1115/1.4063975/1169913>.
- [29] J. Wang, H. Su, K. Chen, D. Du, L. Zhang, Z. Shen, Effect of  $\delta$ -ferrite on the stress corrosion cracking behavior of 321 stainless steel, *Corrosion Sci.* 158 (2019) 108079, <https://doi.org/10.1016/j.corsci.2019.07.005>.
- [30] L. Marchand, M. Derenne, A. Bazergui, Weight loss correlation for sheet gasket materials, *J. Pressure Vessel Technol.* 114 (1992) 1–7, <https://doi.org/10.1115/1.2929007>.
- [31] L. Marchand, A. Bazergui, M. Derenne, Recent developments in elevated temperature gasket evaluation, in: B.S. Nau (Ed.), *Fluid Sealing*, Springer Netherlands, Dordrecht, 1992, pp. 209–223, [https://doi.org/10.1007/978-94-011-2412-6\\_14](https://doi.org/10.1007/978-94-011-2412-6_14).
- [32] ASME B16.5, Pipe Flanges and Flanged Fittings: NPS 1/2 through NPS 24, Metric/Inch Standard, ASME, International, 2021. <https://www.asme.org/codes-standards/find-codes-standards/b16-5-pipe-flanges-flanged-fittings-nps-1-2-nps-24-metric-inch-standard>. (Accessed 25 March 2024).
- [33] ASME B16.21, Nonmetallic Flat Gaskets for Pipe Flanges, ASME, International, 2022. <https://www.asme.org/codes-standards/find-codes-standards/b16-21-no-metallic-flat-gaskets-pipe-flanges>. (Accessed 25 March 2024).
- [34] ASTM G59 - 97, Standard Test Method for Conducting Potentiodynamic Polarization Resistance Measurements, 2020 (n.d.), <https://www.astm.org/Standards/G59>. (Accessed 9 August 2021).
- [35] S. Pourrahimi, L.A. Hof, On the post-processing of complex additive manufactured metallic parts: a review, *Adv. Eng. Mater.* (2024) 2301511, <https://doi.org/10.1002/ADEM.202301511>.
- [36] ASTM A182/A182M-24, Standard Specification for Forged or Rolled Alloy and Stainless Steel Pipe Flanges, Forged Fittings, and Valves and Parts for High-Temperature Service, ASTM International, 2024 [https://compass.astm.org/document/?contentCode=ASTM%7CA0182\\_A0182M-24%7Cen-US&proxycl=https%3A%2F%2Fsecure.astm.org&fromLogin=true](https://compass.astm.org/document/?contentCode=ASTM%7CA0182_A0182M-24%7Cen-US&proxycl=https%3A%2F%2Fsecure.astm.org&fromLogin=true). (Accessed 15 April 2024).
- [37] ASTM G61 - 86, Standard test method for conducting cyclic potentiodynamic polarization measurements for localized corrosion susceptibility of iron-, nickel-, or cobalt-based alloys (n.d.), <https://www.astm.org/Standards/G61.htm>, 2018. (Accessed 28 October 2021).
- [38] R. Baboian, *Corrosion Tests and Standards: Application and Interpretation*, ASTM international, 2005.
- [39] ASTM G102 - 89, e1 Standard Practice for Calculation of Corrosion Rates and Related Information from Electrochemical Measurements (n.d.), <https://www.astm.org/Standards/G102>, 2015. (Accessed 13 November 2021).
- [40] J. Schindelin, I. Arganda-Carreras, E. Frise, V. Kaynig, M. Longair, T. Pietzsch, S. Preibisch, C. Rueden, S. Saalfeld, B. Schmid, J.Y. Tinevez, D.J. White, V. Hartenstein, K. Eliceiri, P. Tomancak, A. Cardona, Fiji: an open-source platform for biological-image analysis, *Nat. Methods* 9 (7 9) (2012) 676–682, <https://doi.org/10.1038/nmeth.2019> (2012).
- [41] B. Cai, Y. Liu, X. Tian, F. Wang, H. Li, R. Ji, An experimental study of crevice corrosion behaviour of 316L stainless steel in artificial seawater, *Corrosion Sci.* 52 (2010) 3235–3242, <https://doi.org/10.1016/j.corsci.2010.05.040>.
- [42] E. Vasilescu, P. Drob, D. Raducanu, I. Cinca, D. Mareci, J.M. Calderon Moreno, M. Popa, C. Vasilescu, J.C. Mirza Rosca, Effect of thermo-mechanical processing on the corrosion resistance of Ti6Al4V alloys in biofluids, *Corrosion Sci.* 51 (2009) 2885–2896, <https://doi.org/10.1016/j.corsci.2009.08.014>.
- [43] J. Qiu, A. Wu, Y. Li, Y. Xu, R. Scarlat, D.D. Macdonald, Galvanic corrosion of Type 316L stainless steel and Graphite in molten fluoride salt, *Corrosion Sci.* 170 (2020) 108677, <https://doi.org/10.1016/j.corsci.2020.108677>.
- [44] B. Mohammadreza Tavakkolizadeh, S. Member, H. Saadatmanesh, Galvanic corrosion of carbon and steel in aggressive environments, *J. Compos. Construct.* 5 (2001) 200–210, [https://doi.org/10.1061/\(ASCE\)1090-0268\(2001\)5:3\(200\)](https://doi.org/10.1061/(ASCE)1090-0268(2001)5:3(200)).
- [45] B. Luo, Q. Hu, J. Liu, F. Huang, Effect of crevice gap on crevice corrosion initiation and development of 2205 duplex stainless steel in NaCl solution, *J. Mater. Res. Technol.* 21 (2022) 2584–2597, <https://doi.org/10.1016/j.jmrt.2022.10.059>.
- [46] E. Shojaei, M. Mirjalili, M.H. Moayed, The influence of the crevice induced IR drop on polarization measurement of localized corrosion behavior of 316L stainless steel, *Corrosion Sci.* 156 (2019) 96–105, <https://doi.org/10.1016/j.corsci.2019.04.030>.
- [47] E. Hornus, K. Wang, M. Pabbruwe, A. Kop, C. Jones, A. Salleh, M. Salasi, M. Iannuzzi, A new experimental method to simulate dynamic crevice corrosion in modular hip arthroplasty, *Corrosion Sci.* 190 (2021), <https://doi.org/10.1016/j.corsci.2021.109704>.
- [48] B. Malki, G. Berthomé, T. Souier, C. Boissy, I. Guillotte, B. Baroux, A combined experimental and computational approach to study crevice corrosion of stainless steels, *J. Electrochem. Soc.* 168 (2021) 101504, <https://doi.org/10.1149/1945-7111/ac2975>.
- [49] C.-J. Park, Y.-H. Lee, Initiation and repassivation of crevice corrosion of type 444 stainless steel in chloride solution, *Met. Mater. Int.* 10 (2004) 447–451.
- [50] G.F. Kennell, R.W. Evitts, K.L. Heppner, A critical crevice solution and IR drop crevice corrosion model, *Corrosion Sci.* 50 (2008) 1716–1725, <https://doi.org/10.1016/j.corsci.2008.02.020>.
- [51] R.S. Lillard, J.R. Scully, Modeling of the factors contributing to the initiation and propagation of the crevice corrosion of alloy 625, *J. Electrochem. Soc.* 141 (1994) 3006–3015, <https://doi.org/10.1149/1.2059273/XML>.
- [52] M.I. Abdulsalam, The role of electrolyte concentration on crevice corrosion of pure nickel, *Mater. Corros.* 58 (2007) 511–513, <https://doi.org/10.1002/MACO.200604037>.
- [53] E. Dhanumalayan, G.M. Joshi, Performance properties and applications of polytetrafluoroethylene (PTFE)—a review, *Adv. Compos. Hybrid Mater.* 1 (2 1) (2018) 247–268, <https://doi.org/10.1007/s42114-018-0023-8>, 2018.
- [54] M. Nishimoto, J. Ogawa, I. Muto, Y. Sugawara, N. Hara, Simultaneous visualization of pH and Cl<sup>-</sup> distributions inside the crevice of stainless steel, *Corrosion Sci.* 106 (2016) 298–302, <https://doi.org/10.1016/j.corsci.2016.01.028>.